The Two-Photon Nondipole Transition Phases Across the Cooper Minima and Resonant States

Baichao Liu[1,2], Yongkun Chen[3*], Chunyang Zhai[2], Qiming Zhao[2], Jiapeng Li[2], Pu Wang[2], Jingkun Xu[2], Qingbin Tang[2], Yingbin Li[2*], Benhai Yu[2], and Yufang Liu[1*]

[1]*Henan Key Laboratory of Infrared Spectrum Measures and Applications, School of Optoelectronic Engineering, Henan Normal University, Xinxiang 453007, China*
[2]*College of Physics and Electronic Engineering, Xinyang Normal University, Xinyang 464000, China*
[3]*School of Physics, Huazhong University of Science and Technology, Wuhan 430074, China*

(Received 21 January 2026; accepted manuscript online 9 March 2026)

Beyond the widely adopted dipole approximation, nondipole effects play an important role in completely understanding the electronic dynamics in light–matter interaction. We present a two-photon interferometric scheme to theoretically study the under-threshold nondipole transition phase over a broad energy range. It is found a significant difference between the nondipole and dipole two-photon transition phases near the Cooper minimum, which originates from the multichannel interference in the nondipole transition. Through the angular dependence of transition phase, we uncover the competition among partial waves in nondipole ionization. This work advances the fundamental understanding of nondipole dynamics in two-photon ionization, and opens a route toward the complete reconstruction of nondipole photoelectron wave packets.

DOI: 10.1088/0256-307X/43/4/040301 CSTR: 32039.14.0256-307X.43.4.040301

Multiphoton ionization is one of the most fundamental quantum processes in laser–matter interaction, which lies at the heart of numerous applications in diverse fields, such as high-harmonic generation,[1,2] two-photon-excited fluorescence microscopy,[3] atmospheric monitoring,[4,5] biochemical sensing,[6] and so on. Two-photon ionization is the simplest multiphoton process. In this process, an electron can absorb one photon to transition to an excited state, followed by ionization via absorption of a second photon, a process known as resonant two-photon ionization. According to perturbation theory, the presence of a resonant state significantly enhances the yield of two-photon ionization. Between two resonant states, the two-photon transition amplitude exhibits a minimum, i.e., an antiresonance or Cooper minimum. Resonances and Cooper minimum endow the photoelectron spectrum with rich spectral features, providing information about atomic and molecular structures. The advent of unique interferometric schemes based on attosecond pulse,[7–9] such as RABBIT (reconstruction of attosecond beating by interference of two-photon transitions),[10] enables direct access to the resonant two-photon transition phase,[11–13] yielding insight into the temporal electron dynamics. RABBIT also serves as a tool for probing the molecular chirality.[14–16] Recently, an energy-resolved extension of the conventional RABBIT method—termed rainbow RABBIT—has been developed.[17] Unlike standard RABBIT, which extracts the phase within a narrow spectral width, rainbow RABBIT utilizes broadband harmonics to simultaneously probe two-photon transition phases over a continuous energy range. This allows for the full reconstruction of the two-photon transition wavepacket,[18] or the characterization of resonant structures and Cooper minima with high spectral resolution.[19]

In multiphoton and two-photon ionization, most physical processes are described within the dipole approximation. However, nondipole effect becomes non-negligible at high photon energies and laser intensities,[20–22] especially in circumstances involving vanishingly small dipole transition, such as at the Cooper minimum,[23,24] electric-quadrupole resonances,[25,26] and zeros of the Fano profile.[27,28] Beyond the dipole approximation, electric-quadrupole and magnetic-dipole transitions obey selection rules different from those of the electric-dipole one, which break down the symmetry of photoelectron yield.[29,30] In single-photon ionization, for example, the electric-quadrupole transition induces a shift in the photoelectron distribution along the light propagation direction.[31] Furthermore, the asymmetric photoelectron yield implies that electrons have a nonzero momentum along the the laser propagation direction, which comes from the photon momentum transfer.[32] Photon momentum transfer has attracted increasing attention in both the multiphoton[33–38] and strong field regime.[35,39–42] Benefiting from advances in experimental techniques and methodologies, recent study has revealed attosecond-resolved nondipole processes in nonlinear photoionization.[43] However, the phase information of nondipole transition via resonant states or Cooper minimum still remains elusive.

In this Letter, we study the nondipole transition in

*Corresponding authors. Email: chenyk@hust.edu.cn; liyingbin2008@163.com; yf-liu@htu.edu.cn
© 2026 Chinese Physical Society and IOP Publishing Ltd. All rights, including for text and data mining, AI training, and similar technologies, are reserved.

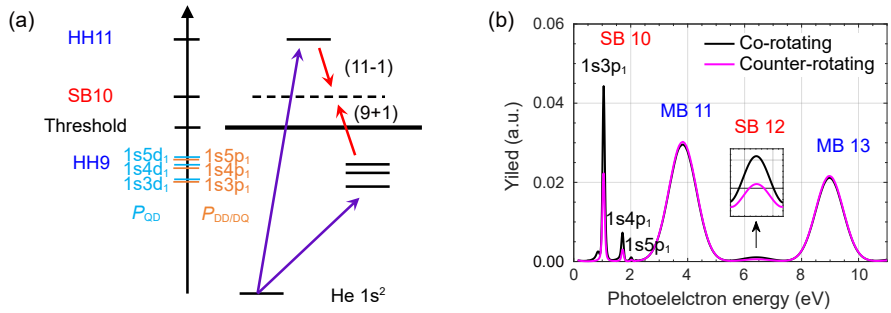

Fig. 1. (a) Illustration of the two-photon ionization channels to SB signals and the intermediate states passed through by the under-threshold dipole ($P_{\rm DD}$) and nondipole ($P_{\rm QD/DQ}$) ionization, staring from the helium ground state ($1s^2$). The two-photon electron wave packet labeled (9+1), created at the SB10 by absorption of the 9th-order harmonic (HH9) and one IR photon, is highly structured because of the intermediate resonant states. The reference wave packet labeled (11-1) is created at the same energy by absorption of HH11 and stimulated emission of an IR photon. (b) Photoelectron spectra for co-rotating (black) and counter-rotating (purple) circularly polarization. Inset: Enlarged view of the spectrum around SB12.

two-photon ionization using the rainbow RABBIT. The results indicate that the nondipole transition phase exhibits jumps at energies corresponding to resonant states and Cooper minima. Due to multichannel interference, the variation of the nondipole transition phase near Cooper minimum is significantly more gradual than that of dipole transition. Furthermore, we find that the photoelectron angular distribution reveals the competition among the partial waves, which provides a route toward distinguishing the contribution of different partial waves in nondipole transitions.

The concept of our scheme is illustrated in Fig. 1(a). We employed a co-rotating or counter-rotating circularly polarized extreme ultraviolet (XUV) attosecond pulse train (APT) and a 480-nm infrared (IR) fields to ionize helium atom, where the IR pulse has a very narrow spectral width and can be treated as monochromatic, whereas the spectrum of individual XUV harmonic is broad, covering excited states over a certain energy range. AN electron absorbing the 9th-order harmonic (HH9; here and throughout, HHn denotes the nth-order harmonic) can transfer to an excited state, followed by absorption of an IR photon to ionize into the continuum at the 10th-order sideband (SB10; here and throughout, SBn denotes the nth-order sideband). Starting from the initial $1s^2$ state, the two-photon dipole transition ($P_{\rm DD}$), induced by the circularly polarized XUV harmonic, proceeds via the $1snp_1$ excited states, and finally generate d_2 (for co-rotating polarization configuration) or s and d_0 waves (for counter-rotating polarization configuration). When the nondipole effect is included, the electric-quadrupole interaction can take place at either the XUV or the IR photon,[44] denoted as the $P_{\rm QD}$ and $P_{\rm DQ}$ channels, respectively. The $P_{\rm DQ}$ channel shares the same intermediate dipole resonant states $1snp_1$ with the $P_{\rm DD}$ channel, because both involve an electric-dipole transition upon XUV photon absorption. The $P_{\rm QD}$ channel, however, undergoes an electronic-quadrupole transition in the first step, restricting it to the nondipole-resonant states $1snd_1$. Despite the intermediate states differ between the $P_{\rm DQ}$ and $P_{\rm QD}$ channels, they produce identical final-state partial waves: f_2 waves for the co-rotating polarization configuration, and p_0 and f_0 waves for the counter-rotating polarization configuration. It should be noted that the magnetic-dipole transition can reasonably be neglected due to the weak contribution.[44] The wave packet labeled (11-1), created by absorption of HH11 and stimulated emission of an IR photon, serves as a reference wave at the same energy.

We obtained the photoelectron spectrum by numerically solving the three-dimensional Schrödinger equation (TDSE),[45] as shown in Fig. 1(b). In our simulation, the TDSE is solved within the single-active-electron approximation by the split-operator method.[43,46,47] For He atom, we used a one-electron effective potential described by $V(\boldsymbol{r}) = -\left[1 + \exp\left(-2.1325r\right)\right]/r$.[48] We use a 480-nm IR field ($\omega = 0.095$ a.u.), which has a Gaussian envelope with a duration of 128 fs. The XUV APT contains odd-order harmonics from HH3 (7.75 eV) to HH25 (64.60 eV), where the attosecond pulses have the Gaussian envelopes with the full width at half-maximum (FWHM) durations of 80 as, and the APT has a Gaussian envelope with a FWHM duration of 1.6 fs. The peak intensities of the IR and XUV pulse are 5×10^{11} and 5×10^{13} W/cm^2, respectively. The single XUV APT envelope duration of 1.6 fs is chosen to provide sufficient spectral bandwidth to cover multiple resonant states and the peak intensity of the XUV pulse is selected to ensure that the two-photon sideband signals are clearly visible while remaining within the perturbative regime. For our laser parameters, the TDSE is solved within a spherical box of radius $R_{\rm max} = 320$ a.u. and radial grid points of 160. The quantum numbers of partial waves are up to $l_{\rm max} = 10$ and $m_{\rm max} = 10$. All these parameters have been carefully verified to ensure numerical convergence. Electron–electron correlation, while important for certain processes such as double ionization,[49,50] is not the focus of this work and is therefore excluded from our calculation.

In Fig. 1(b), the yield of sideband SB12, formed by above-threshold two-photon ionization, is significantly lower than that of the 11th- and 13th-order main bands produced by single-photon ionization, and its energy spectrum exhibits a Gaussian profile. In contrast, the yield of

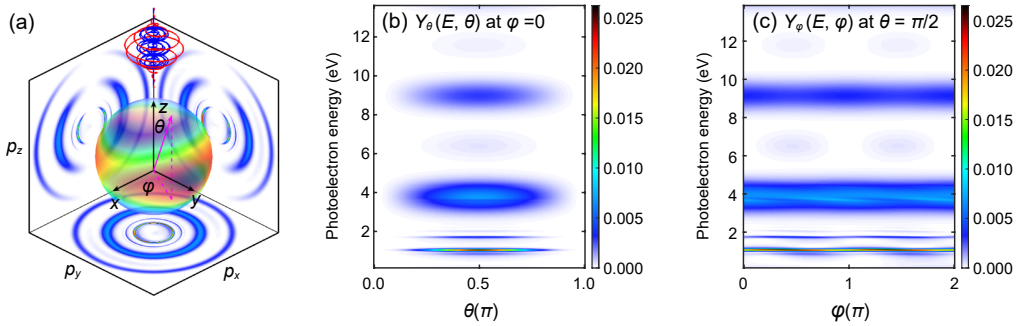

Fig. 2. (a) Three-dimensional PMD. A left-hand circularly polarized XUV APT and a co-rotating/counter-rotating IR field are employed to ionize helium, with the z axis aligned along the propagation direction and the xy plane corresponding to the polarization plane. (b) and (c) PMD in the xz and xy planes, respectively, for the co-rotating polarization configuration.

SB10, which involves the under-threshold two-photon ionization, exceeds that of the main bands. Furthermore, the spectrum of SB10 exhibits highly structured, because of the intermediate resonant state. These peaks correspond to the resonant states involved in the under-threshold two-photon ionization. By analyzing the photoelectron energies of these resonant peaks, we identify that these three peaks observed at SB10 correspond to the $1s3p_1$, $1s4p_1$, and $1s5p_1$ resonant states of the helium atom. Their binding energies are 1.538 eV, 0.862 eV, and 0.550 eV, respectively, in excellent agreement with the NIST tabulated values (1.580 eV, 0.880 eV, and 0.559 eV). Additionally, under the co-rotating polarization configuration, a small subsidiary peak appears on the left side of the peak corresponding to the $1s3p_1$ state, which is absent in the case of the counter-rotating circularly polarization. Currently, we do not have a definitive explanation for this phenomenon, and it is not the focus of this paper.

Figure 2(a) displays the three-dimensional photoelectron momentum distribution (PMD), where the angular dependence of photoelectrons encodes the underlying photoionization dynamics. The PMD in the xz and xy planes for the co-rotating polarization configuration are presented in Figs. 2(b) and 2(c), respectively. In xz plane, a weak forward-backward asymmetry in the PMD appears at SB10. This is a direct manifestation of the nondipole effect.[24,32] Specifically, the partial waves of dipole (s, d_0, d_2) and nondipole (p_0, f_0, f_2) channels have opposite parities; their coherent quantum interference induces a forward-backward asymmetric photoelectron distribution along the light propagation direction. Furthermore, as a consequence of the selection rules unde circularly polarized IR pulse, electrons absorbing an IR photon and those emitting one acquire final magnetic quantum numbers differing by 2. Consequently, interference between the emission and absorption channels gives rise to photoemission anisotropy in the xy plane, i.e., the photoelectron yield at SBs exhibits 2φ-modulation, described by $\mathcal{I} \propto A + B\cos(2\varphi + \Delta\phi)$, where $\mathcal{I}$ is the photoelectron yield and φ is the azimuth angle. The modulation phase $\Delta\phi$ imprints the two-photon transition phase via intermediate resonant states, providing information on photoionization dynamics without scanning the XUV-IR time delay.[51–54]

To isolate the contribution of nondipole partial waves, we introduce the asymmetry signal,

$$\begin{aligned}&\mathcal{A}(E,\theta,\varphi)\\ =\;&\frac{\mathcal{I}(E,\theta,\varphi)-\mathcal{I}(E,\pi-\theta,\varphi)}{2}\\ =\;&\mathcal{A}_0(E,\theta)+\mathcal{A}_1(E,\theta)\cos\left[2\varphi-\Delta\phi_{\mathcal{A}}(E,\theta)\right],\end{aligned}\tag{1}$$

where $\mathcal{I}(E,\theta,\varphi)$ is the photoelectron yields at the SB signal of energy E and at the emission direction (θ,φ), with θ and φ being polar and azimuthal angles, respectively. This asymmetry signal eliminates the symmetric background signal and only contains the coherent interference of even- and odd-parity partial waves, which enables the extraction of two-photon nondipole transition phases. Likewise, we introduce the forward-backward symmetry signal,

$$\begin{aligned}&\mathcal{S}(E,\theta,\varphi)\\ =\;&\frac{\mathcal{I}(E,\theta,\varphi)+\mathcal{I}(E,\pi-\theta,\varphi)}{2}\\ =\;&\mathcal{S}_0(E,\theta)+\mathcal{S}_1(E,\theta)\cos\left[2\varphi-\Delta\phi_{\mathcal{S}}(E,\theta)\right],\end{aligned}\tag{2}$$

which removes the contribution of asymmetric signal and separates out the coherent interference between the partial waves from the dipole transition. In our simulation, there is no chirped effect in either XUV APT or IR pulse, thus the modulation phases $\Delta\phi_{\mathcal{A}/\mathcal{S}}(E,\theta)$ are the relative phase of the photoelectron wave packet of emission channels wherein partial waves interfere coherently, with respect to that of absorption channels. In experimental implementations, the chirp of the XUV or IR pulses would introduce additional phase contributions, which can be characterized independently and subtracted using established calibration techniques.[10] Figures 3(a) and 3(c) display the polar angle-energy resolved asymmetry and symmetry signals

$$\mathcal{A}_\theta(E,\theta)=\int_0^{2\pi}\mathcal{A}(E,\theta,\varphi)\,\mathrm{d}\varphi=\mathcal{A}_0(E,\theta),\tag{3a}$$

$$\mathcal{S}_\theta(E,\theta)=\int_0^{2\pi}\mathcal{S}(E,\theta,\varphi)\,\mathrm{d}\varphi=\mathcal{S}_0(E,\theta)\tag{3b}$$

at SB10 for co-rotating polarization configuration, respectively. The results indicate that the yield of the asymmetry signal including nondipole partial waves is two to three orders of magnitude lower than that of the symmetry

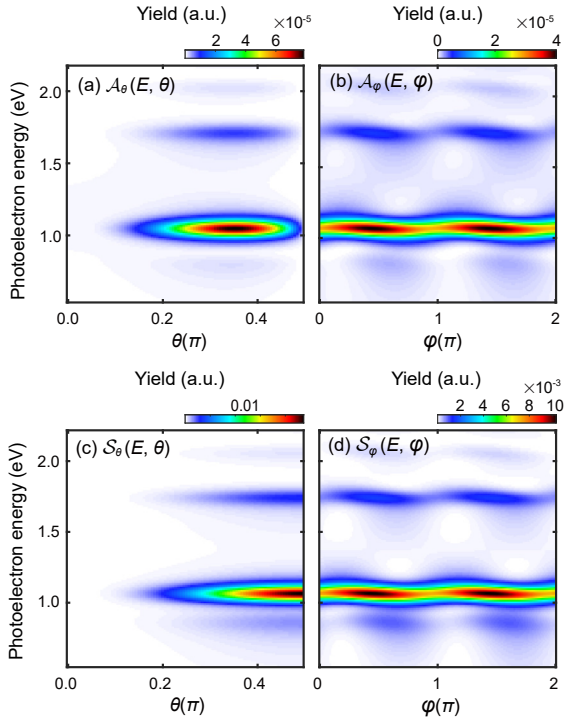

Fig. 3. (a) Polar angle- and (b) azimuth angle-energy-resolved asymmetry signal at SB10 for the co-rotating polarization configuration. (c) and (d) Same as (a) and (b), respectively, but for the symmetry signal.

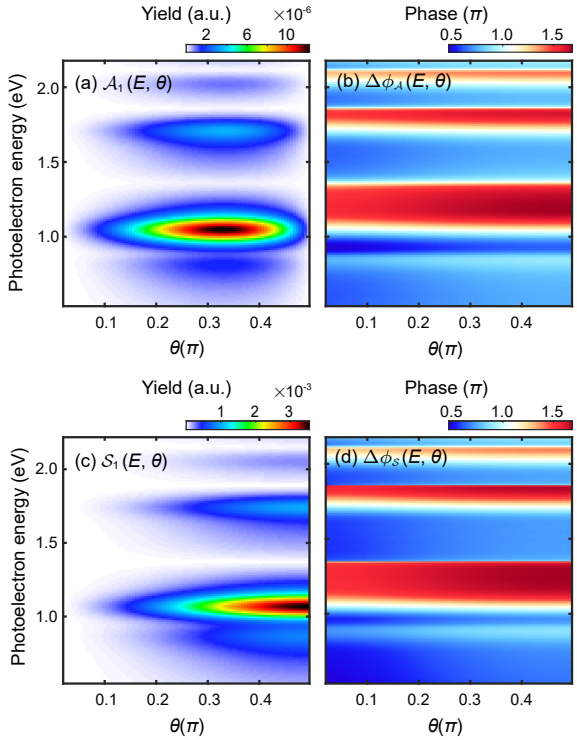

Fig. 4. (a) Modulation amplitude and (b) phase of asymmetry signal at SB10 as a function of photoemission polar angles θ and photoelectron energy for co-rotating polarization configuration. (c), (d) Same as (a), (b) but for symmetry signal.

signal which only contains dipole partial waves, owing to the much smaller transition amplitude of nondipole channels compared to dipole transitions. Furthermore, pronounced resonance peaks are observed for both the asymmetry and symmetry signals. The azimuth angle-energy resolved asymmetry and symmetry signals,

$$\mathcal{A}_\varphi(E, \varphi) = \int_0^{\frac{\pi}{2}} \mathcal{A}(E, \theta, \varphi)\, \mathrm{d}\theta, \tag{4a}$$

$$\mathcal{S}_\varphi(E, \varphi) = \int_0^{\frac{\pi}{2}} \mathcal{S}(E, \theta, \varphi)\, \mathrm{d}\theta, \tag{4b}$$

are also shown in Figs. 3(b) and 3(d), respectively. The photoelectron yields of both signals exhibit the 2φ-modulation, as we mentioned previously. It can be seen that the modulation phase shows an evident variation with photoelectron energy and changes rapidly near the resonant peaks.

Figure 4 shows the modulation amplitudes and phases of the asymmetry and symmetry signals for the co-rotating polarization configuration. The polar angle-energy-resolved modulation amplitudes of the asymmetry and symmetry signals are similar to $\mathcal{A}_\theta(E, \theta)$ and $\mathcal{A}_\theta(E, \theta)$ shown in Fig. 3, but with more pronounced resonance peaks. At energies corresponding to the extrema, i.e., Cooper minima or resonance peaks, of the modulation amplitude $\mathcal{A}/\mathcal{S}_1(E, \theta)$, the modulation phase $\Delta\phi_{\mathcal{A}/\mathcal{S}}(E, \theta)$ exhibits an abrupt jump of approximately π, which stems from the sign reversal of two-photon transition matrix element. Within low-order perturbation theory, the two-photon transition matrix element in RABBIT can be described as

$$\mathcal{M} \propto \sum_\nu \frac{\langle \psi_f | \hat{O} | \psi_\nu \rangle \langle \psi_\nu | \hat{O} | \psi_i \rangle}{\omega_i + \Omega - \omega_\nu + \mathrm{i}0^+}. \tag{5}$$

Here, $\hat{O}$ is the transition operator and Ω is the frequency of XUV harmonic. $|\psi\rangle$ is the eigenstate of Hamiltonian, where the subscripts i, ν, and f represent the initial, intermediate, and final states, respectively. ω_i and ω_ν are the energies of the initial and intermediate states. At the energy corresponding to a resonant intermediate state, the denominator of the two-photon transition matrix element passes through zero ($\omega_i + \Omega = \omega_\nu$), causing the transition amplitude to reach a maximum and the transition phase to undergo a jump. Between two adjacent resonances, two contributions with opposite signs dominate the transition matrix element. These contributions cancel each other at a specific energy, leading to a local minimum in the transition amplitude—known as the Cooper minimum—and a π jump in the transition phase. To highlight this, figure 5(a) presents the modulation phases of the asymmetry and symmetry signals as functions of photoelectron energy. The resonance state leads to an increase jump of π of the modulation phase, whereas the decrease of π of the modulation phase is caused by the Cooper minimum. It is evident that the symmetry signal displays a steeper slope in its phase jump than the asymmetry signal near the dipole Cooper minimum (around 1.36 eV), which leads to a large phase difference between the asymmetry and symmetry signals [Fig. 5(b)].

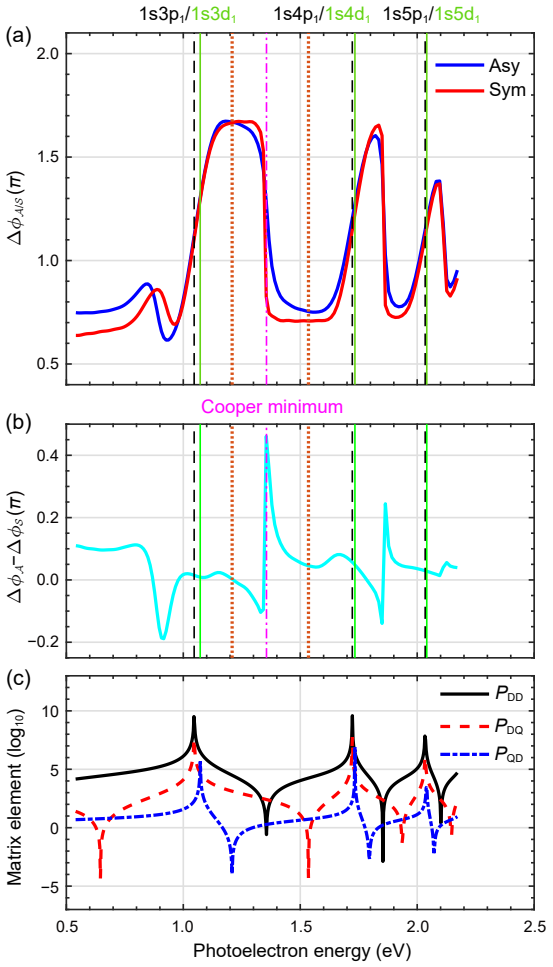

Fig. 5. (a) Modulation phases of asymmetry (red curve) and symmetry (blue curve) signals, averaged over $\theta \in [\pi/3, 4\pi/9]$, as a function of photoelectron energy. (b) Difference between the modulation phases of the asymmetry and symmetry signals. (c) Radial transition matrix elements of P_{DD} (black solid curve), P_{DQ} (red dashed curve), and P_{QD} (blue dotted curve) channels. The vertical lines represent the energies corresponding to dipole (black dashed lines) and nondipole (green solid lines) resonance states, as well as the Cooper minima of dipole channel (violet dot dashed line) and nondipole channels (brown dotted lines).

This difference originates from the non-zero but small contributions of nondipole channels near the dipole Cooper minimum. The dipole channel P_{DD} proceeds only through one Cooper minimum at 1.36 eV [Fig. 5(c)], resulting in a decrease jump of the modulation phase at a single energy. However, the nondipole transitions, either the P_{DQ} channel or the P_{QD} channel, exhibit the Cooper minima located away from 1.36 eV (1.54 eV for P_{DQ} and 1.21 eV for P_{QD}). Consequently, the dipole and nondipole channels have decrease phase jumps at different energies, and the coherent interference between those channels produces a broader, more gradual phase variation in the asymmetry signal. As the photoelectron energy increases, the Cooper minima traversed by the dipole and nondipole transitions gradually approach a common energy, and the overall phase-jump slope of the asymmetry signal steepens. On the other hand, due to the small energy difference between the dipole and nondipole resonant states, the modulation phase difference between the asymmetry and symmetry signal is not obvious near the resonance energies.

It should be noted that we focuses exclusively on under-threshold intermediate resonances, which dominate the two-photon ionization yield in the near-threshold regime. Above-threshold resonances, such as autoionizing states, are expected to introduce additional phase variations and Fano-type line shapes.[55] However, they do not affect the results of our work and are therefore not addressed here.

We further calculated the PMD for the counter-rotating polarization configuration, as shown in Fig. 6. Besides the three visible resonance peaks, both the average value of modulation and the modulation amplitude exhibit a minimum around $\theta = 0.2\pi$, and the modulation phase shows a corresponding jump of approximately π at the same angular position. This behavior results from the quantum interference among partial waves, and the markedly different angular distribution compared with that for the co-rotating polarization configuration (Fig. 4) stems from differences in the dominant partial-wave components between the two configurations.

Within the under-threshold RABBIT framework, the presence of resonant states leads to a much larger contribution of the absorption channel than that of the emission channel. In the co-rotating polarization configuration, the (9+1) wave packet involves the dipole partial wave d_2 and nondipole partial wave f_2, where the d_2 wave exhibits a two-lobed shape in the polar angle with a maximum at $\theta = \pi/2$ and a minimum at $\theta = 0$. This angular distribution agrees with the polar angle-energy-resolved average value [Fig. 3(c)] and modulation amplitude [Fig. 4(c)] of the symmetry signal. Similarly, the f_2 wave exhibits a four-lobed shape in the polar angle, with a maximum around $\theta = 0.3\pi$ and nodes at $\theta = 0$ and π, in agreement with the polar angular distribution of the asymmetry signal [Figs. 3(a) and 4(a)]. While the absorption channel induced by the counter-rotating polarized XUV and IR pulses produces s and d_0 waves for dipole transition and p_0 and f_0 waves for nondipole transition. Here, s wave is isotropic; d_0, p_0, and f_0 waves exhibit four-lobed, two-lobed, and six-lobed structures, respectively. The increase in these prominent partial waves significantly enriches the photoelectron angular distribution. In particular, the dominant contributions of d_0 and f_0 waves result in a node of the photoelectron angular distribution near $\theta = 0.2\pi$. The photoelectron angular distribution encodes the amplitude and phase information of individual partial waves. By decomposing the measured two-photon transition amplitudes and phases into partial-wave components—using, for instance, partial-wave expansion[18]—it is in principle possible to isolate the contributions from different partial waves and reconstruct the complete quantum wave packet of the nondipole photoelectron. Such a reconstruction would provide access to the temporal and spatial structure of continuum electron dynamics beyond the dipole approximation.

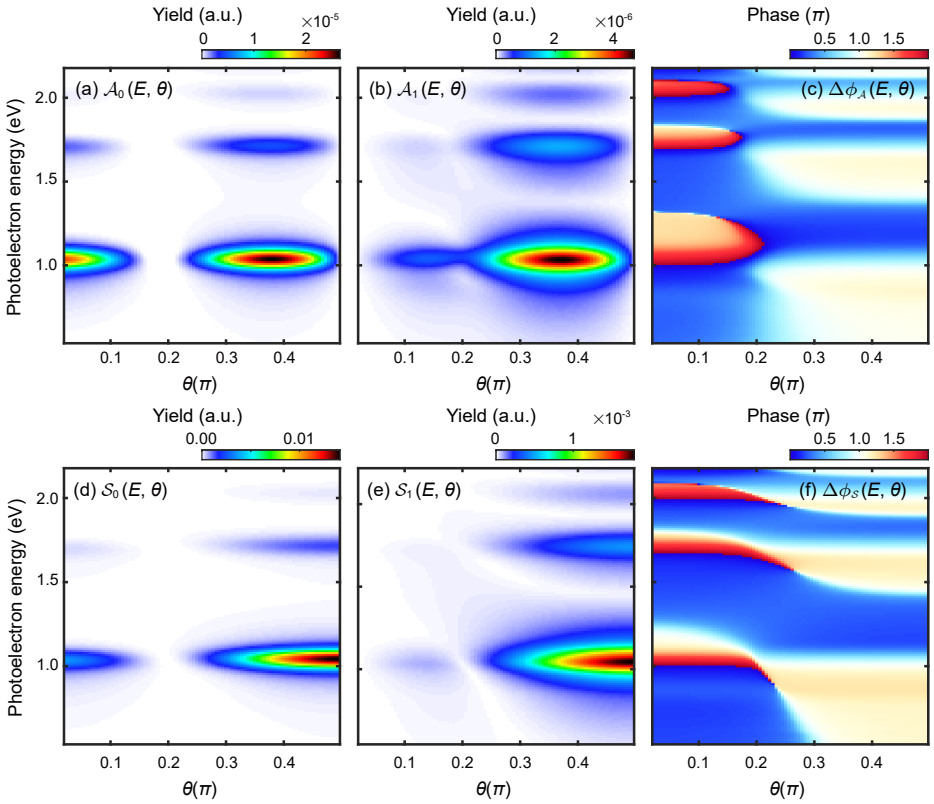

Fig. 6. (a) Average value $\mathcal{A}_0(E, \theta)$, (b) modulation amplitude $\mathcal{A}_1(E, \theta)$, and (c) modulation phase $\Delta\phi_{\mathcal{A}}(E, \theta)$ of asymmetry signal [Eq. (1)] at SB10 as function of polar angle and photoelectron energy for the counter-rotating polarization configuration. (d)–(f) Same as (a)–(c), respectively, but for symmetry signal [Eq. (2)].

In summary, we theoretically study the nondipole transition phase in the under-threshold two-photon ionization. Beyond the dipole approximation, due to the non-zero contributions of nondipole channels near the dipole Cooper minimum, the resulting nondipole transition phase varies more gradually than that of the dipole transition. Moreover, we find that the significant difference in photoelectron yield between the co-rotating and counter-rotating polarization configurations stems from the distinct of dominant partial waves for these two contributions. In particular, for the counter-rotating polarization configuration, competition among the primary partial waves (d_0 and f_0) leads to an abrupt jump of modulation phase near $\theta = 0.2\pi$. Our work reveals how Cooper minimum manifests in the modulation phase and how partial-wave contributions affect the angular dependence of the photoelectron yield. These results advance the fundamental understanding of nondipole dynamics in two-photon ionization and open a path toward the complete reconstruction of nondipole photoelectron wave packets.

The sensitivity of the two-photon nondipole transition phase to resonant and near-minimum regions suggests a possible route for coherent control. By tailoring the parameters of the driven fields, one could selectively enhance or suppress specific partial-wave contributions, thereby control the angular and temporal structure of the total photoelectron wave packet. This opens up opportunities for phase-controlled nondipole interferometry and quantum control in the multiphoton regime.

Acknowledgements. This work was supported by the National Natural Science Foundation of China (Grant Nos. 12574316, 12504323, 12504329, and 12547161), the Key Scientific Research Projects of Higher Education Institutions of Henan Province (Grant No. 26A140011), and the Nanhu Scholars Program for Young Scholars of Xinyang Normal University.

References

[1] Schafer K J, Yang B, DiMauro L F, and Kulander K C 1993 *Phys. Rev. Lett.* **70** 1599
[2] Corkum P B 1993 *Phys. Rev. Lett.* **71** 1994
[3] Denk W, Strickler J H, and Webb W W 1990 *Science* **248** 73
[4] Xu H, Cheng Y, Chin S L, and Sun H B 2015 *Laser Photonics Rev.* **9** 275
[5] Li H, Chu W, Xu H, Cheng Y, Chin S L, Yamanouchi K, and Sun H B 2016 *Sci. Rep.* **6** 27340
[6] Chin S L, Xu H L, Luo Q *et al.* 2009 *Appl. Phys. B* **95** 1
[7] Paul P M, Toma E S, Breger P, Mullot G, Augé F, Balcou Ph, Muller H G, and Agostini P 2001 *Science* **292** 1689
[8] Chen J Q, Jiang W L, Qiao Y, Yang Y J, and Chen J G 2025 *Chin. Phys. Lett.* **42** 013201
[9] Zheng Z G, Wang L, Wang D, Wang M Y, Xiao F, Zhao J, Wang X, and Zhao Z X 2025 *Chin. Phys. Lett.* **42** 090302
[10] Klünder K, Dahlström J M, Gisselbrecht M *et al.* 2011 *Phys. Rev. Lett.* **106** 143002
[11] Swoboda M, Fordell T, Klünder K, Dahlström J M, Miranda M, Buth C, Schafer K J, Mauritsson J, L'Huillier A, and Gisselbrecht M 2010 *Phys. Rev. Lett.* **104** 103003

[12] Villeneuve D M, Hockett P, Vrakking M J J, and Niikura H 2017 *Science* **356** 1150
[13] Drescher L, Witting T, Kornilov O, and Vrakking M J J 2022 *Phys. Rev. A* **105** L011101
[14] Beaulieu S, Comby A, Clergerie A *et al.* 2017 *Science* **358** 1288
[15] Djiokap J M N 2023 *Nat. Phys* **19** 154
[16] Zhou Z, Li Y, Zhang X, Zhou Y, and Lu P 2026 *Adv. Photonics* **8** 015001
[17] Gruson V, Barreau L, Jiménez Galan Á *et al.* 2016 *Science* **354** 734
[18] Autuori A, Platzer D, Lejman M *et al.* 2022 *Sci. Adv.* **8** eabl7594
[19] Neoričić L, Busto D, Laurell H *et al.* 2022 *Front. Phys.* **10** 964586
[20] Hemmers O, Guillemin R, and Lindle D W 2004 *Radiat. Phys. Chem.* **70** 123
[21] Maurer J and Keller U 2021 *J. Phys. B* **54** 094001
[22] Dou Y, Fang Y, Ge P, and Liu Y 2023 *Chin. Phys. Lett.* **40** 033201
[23] Pradhan G B, Jose J, Deshmukh P C, LaJohn L A, Pratt R H, and Manson S T 2011 *J. Phys. B* **44** 201001
[24] Ilchen M, Hartmann G, Gryzlova E V *et al.* 2018 *Nat. Commun.* **9** 4659
[25] Lambropoulos P, Doolen G, and Rountree S P 1975 *Phys. Rev. Lett.* **34** 636
[26] Lambropoulos M, Moody S E, Smith S J, and Lineberger W C 1975 *Phys. Rev. Lett.* **35** 159
[27] Martin N L S, Thompson D B, Bauman R P, Caldwell C D, Krause M O, Frigo S P, and Wilson M 1998 *Phys. Rev. Lett.* **81** 1199
[28] Dolmatov V K and Manson S T 1999 *Phys. Rev. Lett.* **83** 939
[29] Cooper J W 1990 *Phys. Rev. A* **42** 6942
[30] Cooper J W 1993 *Phys. Rev. A* **47** 1841
[31] Krause M O 1969 *Phys. Rev.* **177** 151
[32] Grundmann S, Kircher M, Vela Perez I *et al.* 2020 *Phys. Rev. Lett.* **124** 233201
[33] Chelkowski S, Bandrauk A D, and Corkum P B 2014 *Phys. Rev. Lett.* **113** 263005
[34] Chelkowski S, Bandrauk A D, and Corkum P B 2017 *Phys. Rev. A* **95** 053402
[35] He P L, Lao D, and He F 2017 *Phys. Rev. Lett.* **118** 163203
[36] Wang M X, Xiao X R, Liang H, Chen S G, and Peng L Y 2017 *Phys. Rev. A* **96** 043414
[37] Liang H, Wang M X, Xiao X R, Gong Q, and Peng L Y 2018 *Phys. Rev. A* **98** 063413
[38] Wang M X, Liang H, Xiao X R, Chen S G, and Peng L Y 2019 *Phys. Rev. A* **99** 023407
[39] Smeenk C T L, Arissian L, Zhou B, Mysyrowicz A, Villeneuve D M, Staudte A, and Corkum P B 2011 *Phys. Rev. Lett.* **106** 193002
[40] Liu J, Xia Q Z, Tao J F, and Fu L B 2013 *Phys. Rev. A* **87** 041403
[41] Ludwig A, Maurer J, Mayer B W, Phillips C R, Gallmann L, and Keller U 2014 *Phys. Rev. Lett.* **113** 243001
[42] Chen S G, Jiang W C, Grundmann S, Trinter F, Schöffler M S, Jahnke T, Dörner R, Liang H, Wang M X, Peng L Y, and Gong Q 2020 *Phys. Rev. Lett.* **124** 043201
[43] Liang J, Han M, Liao Y, Ji J B, Leung C S, Jiang W C, Ueda K, Zhou Y, Lu P, and Wörner H J 2024 *Nat. Photon.* **18** 311
[44] Liao Y, Chen Y, Dahlström J M, Pi L W, Lu P, and Zhou Y 2024 *Phys. Rev. A* **110** 023109
[45] Geng L, Liang H, and Peng L Y 2022 *Chin. Phys. Lett.* **39** 044203
[46] Liang J, Zhou Y, Liao Y, Jiang W C, Li M, and Lu P 2022 *Ultrafast Sci.* **2022** 9842716
[47] Jiang W C and Tian X Q 2017 *Opt. Express* **25** 26832
[48] Muller H G 1999 *Phys. Rev. A* **60** 1341
[49] Li Y, Qin L, Liu A, Zhang K, Tang Q, Zhai C, Xu J, Chen S, Yu B, and Chen J 2022 *Chin. Phys. Lett.* **39** 093201
[50] Li Y, Wu F, Liu F, Kang S, Li Z, Zhang K, Liu Y, Li K, Zhai C, Xu J, Wang P, Zhao Q, and Yu B 2025 *Chin. Phys. Lett.* **42** 053703
[51] Donsa S, Douguet N, Burgdörfer J, Březinov'a I, and Argenti L 2019 *Phys. Rev. Lett.* **123** 133203
[52] Sörngård J, Dahlström J M, and Lindroth E 2020 *J. Phys. B* **53** 134003
[53] Han M, Ji J B, Ueda K, and Wörner H J 2023 *Optica* **10** 1044
[54] Han M, Ji J B, Balčiūnas T, Ueda K, and Wörner H J 2023 *Nat. Phys.* **19** 230
[55] Fano U 1961 *Phys. Rev.* **124** 1866